New analytical threshold voltage model for halo-doped cylindrical surrounding-gate MOSFETs*

Li Cong(李聪)[1,†], Zhuang Yiqi(庄奕琪)[1], and Han Ru(韩茹)[2]

[1]Key Laboratory for Wide Band-Gap Semiconductor Materials and Devices of Ministry of Education, School of Microelectronics, Xidian University, Xi'an 710071, China
[2]Aviation Microelectronics Center, Northwestern Polytechnic University, Xi'an 710072, China

Abstract: Using an exact solution of two-dimensional Poisson's equation in cylindrical coordinates, a new analytical model comprising electrostatic potential, electric field, threshold voltage and subthreshold current for halo-doped surrounding-gate MOSFETs is developed. It is found that a new analytical model exhibits higher accuracy than that based on parabolic potential approximation when the thickness of the silicon channel is much larger than that of the oxide. It is also revealed that moderate halo doping concentration, thin gate oxide thickness and small silicon channel radius are needed to improve the threshold voltage characteristics. The derived analytical model agrees well with a three-dimensional numerical device simulator ISE.

Key words: MOSFETs; cylindrical surrounding-gate; threshold voltage; analytical model; halo

DOI: 10.1088/1674-4926/32/7/074002 **PACC:** 7340Q; 1240Q; 7360J

1. Introduction

One of the major issues with the scaling down of the classical MOSFETs is the control of short-channel effects (SCEs), such as threshold voltage roll-off, drain-induced barrier lowering (DIBL) and hot-carrier effects (HCEs)[1]. In order to extend the scalability of MOSFET technology, a variety of nonclassical MOSFET structures have been proposed. Among them, the cylindrical surrounding-gate (CSG) MOSFET is considered to be one of the most promising candidates owing to its excellent control of the channel[2−10]. However, even in CSG MOSFETs, SCEs and HCEs cannot be neglected for channel lengths below 100 nm[4].

To enhance the immunity against SCEs and HCEs of CSG, symmetric halo-doped cylindrical surrounding-gate (HSG) MOSFETs have been proposed by Li[6]. His work shows that the halo doping profile exhibits better performance in suppressing threshold voltage roll-off, drain-induced barrier lowering, and increasing carrier transport efficiency. The threshold voltage model based on parabolic potential approximation (PPA) was also proposed by him. PPA assumes a parabolic potential function in the radial direction, thereby ignoring the affection of other two-dimensional (2D) function. Large errors occur when the thickness of silicon is much larger than that of the oxide[11].

To precisely analyze the HSG MOSFETs, the rigorous analytical expressions without PPA are derived based on the exact solution of Poisson's equation in cylindrical coordinates, comprising models for channel electrostatic potential, electric field, threshold voltage and subthreshold current. Those models are also compatibly used to simulate other kinds of CSG MOSFETs with one, two or three continuous channel regions. The model results are verified by comparing them with simulated results obtained from the three-dimensional (3D) numerical device simulator ISE.

2. Analytical model

A schematic cross-sectional view of an HSG MOSFET is shown in Fig. 1. The halo doping concentration N_{h} is higher than the doping concentration N_{c} in the rest of the channel. Considering the device structure, the channel can be divided into three regions. The lengths of the three regions are L_1, L_2 and L_3, respectively. Owing to the cylindrical symmetry of the device structure, a cylindrical coordinate system is employed, which consists of a radial direction r and a horizontal direction z (angular component θ is not shown in the figure). The symmetry of the structure ensures that the potential and the electric field have no variation with angle in the plane of the radial direction. Hence, a 2D analysis is sufficient.

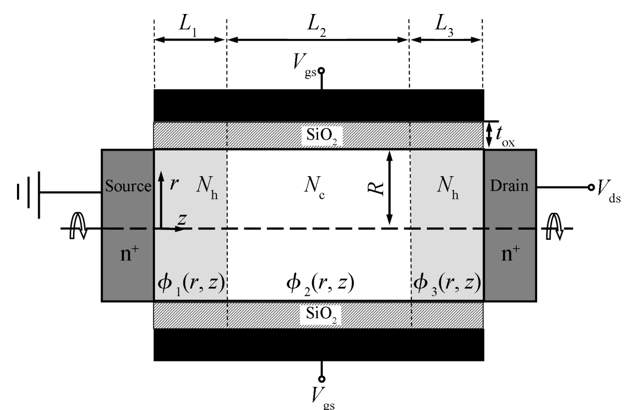

Fig. 1. Schematic cross-section of halo-doped surrounding-gate MOSFETs.

* Project supported by the National Natural Science Foundation of China (No. 61076101).
† Corresponding author. Email: cong.li@mail.xidan.edu.cn
Received 6 December 2010, revised manuscript received 8 March 2011
© 2011 Chinese Institute of Electronics

2.1. Potential model

The electrostatic potential and electric field distribution in the silicon channel can be derived by solving Poisson's equation. Assuming that the influence of charge carriers and fixed charges on the electrostatics of the channel can be neglected, the silicon channel is fully depleted, then the electrostatic potential $\phi(r,z)$ in three regions of the channel can be written as

$$\frac{1}{r}\frac{\partial}{\partial r}\left(r\frac{\partial}{\partial r}\phi_1(r,z)\right)+\frac{\partial^2}{\partial z^2}\phi_1(r,z)=\frac{qN_1}{\varepsilon_{\rm si}},\quad 0\leqslant z\leqslant L_1,\quad 0\leqslant r\leqslant R,$$

$$\frac{1}{r}\frac{\partial}{\partial r}\left(r\frac{\partial}{\partial r}\phi_2(r,z)\right)+\frac{\partial^2}{\partial z^2}\phi_2(r,z)=\frac{qN_2}{\varepsilon_{\rm si}},\quad L_1\leqslant z\leqslant L_1+L_2,\quad 0\leqslant r\leqslant R,$$

$$\frac{1}{r}\frac{\partial}{\partial r}\left(r\frac{\partial}{\partial r}\phi_3(r,z)\right)+\frac{\partial^2}{\partial z^2}\phi_3(r,z)=\frac{qN_3}{\varepsilon_{\rm si}},\quad L_1+L_2\leqslant z\leqslant L,\quad 0\leqslant r\leqslant R,\tag{1}$$

where q is the electron charge, $N_1=N_{\rm h}$, $N_2=N_{\rm c}$, $N_3=N_{\rm h}$, $\varepsilon_{\rm si}$ is the dielectric constant of the silicon channel, $L=L_1+L_2+L_3$ is the total gate length and $\phi_j(r,z)(j=1,2,3)$ is the potential distribution in region j. Using the superposition technique, the electrostatic potential in each region of the silicon channel can be expressed as

$$\phi_j(r,z)=V_j(r,z)+W_j(r),\quad j=1,2,3,\tag{2}$$

where $W_j(r)$ is the one-dimensional (1D) solution to Poisson's equation, while $V_j(r,z)$ is the 2D solution to the homogeneous Laplace equation with a third boundary condition, i.e.,

$$\frac{\partial^2}{\partial r^2}W_j(r)+\frac{1}{r}\frac{\partial}{\partial r}W_j(r)=\frac{qN_j}{\varepsilon_{\rm si}},\quad j=1,2,3,\tag{3}$$

$$\frac{\partial^2}{\partial r^2}V_j(r,z)+\frac{1}{r}\frac{\partial}{\partial r}V_j(r,z)+\frac{\partial^2}{\partial z^2}V_j(r,z)=0,\quad j=1,2,3.\tag{4}$$

In HSG MOSFETs, the electric field in the center of the silicon channel is zero by symmetry

$$\left.\frac{\partial\phi_j(r,z)}{\partial r}\right|_{r=0}=0,\quad j=1,2,3,\tag{5}$$

and the electric flux at the interface between the gate dielectric and the silicon channel is continuous

$$\varepsilon_{\rm si}\left.\frac{\partial\phi_j(r,z)}{\partial r}\right|_{r=R}=\frac{\varepsilon_{\rm ox}}{t'_{ox}}[V_{\rm gs}-\phi_{\rm MS}-\phi_j(r=R,z)],\quad j=1,2,3,\tag{6}$$

where $t'_{\rm ox}=R\ln(1+t_{\rm ox}/R)$ is the equivalent oxide thickness[2]. The work function difference $\phi_{\rm MS}$ is given as

$$\phi_{\rm MS}=\phi_{\rm M}-\phi_{\rm si},\tag{7}$$

in which, $\phi_{\rm M}$ is the metal work functions. $\phi_{\rm si}$ is the silicon work function of halo regions, which can be written as

$$\phi_{\rm si}=\chi_{\rm si}+\frac{E_{\rm g}}{2q}+\phi_{\rm Fh},\tag{8}$$

where

$$\phi_{\rm Fh}=\frac{kT}{q}\ln\frac{N_{\rm h}}{n_{\rm i}}\tag{9}$$

is the Fermi potential of the halo region, $E_{\rm g}$ is the silicon band gap, $\chi_{\rm si}$ is the electron affinity, and $n_{\rm i}$ is the intrinsic carrier concentration.

From Eqs. (3)–(6), the solutions for $W_j(r)$ can be obtained as

$$W_j(r)=\frac{qN_j}{4\varepsilon_{\rm si}}r^2+V_{\rm gs}-\phi_{\rm MS}-\frac{qN_jt'_{\rm ox}R}{2\varepsilon_{\rm ox}}-\frac{qN_jR^2}{4\varepsilon_{\rm si}},\quad j=1,2,3.\tag{10}$$

Using the separation method, one obtains the general solution for $V_j(r,z)$ in the form of the Fourier-Bessel series, i.e.,

$$V_j(r,z)=\sum_{n=1}^{\infty}\left[C_n^{(j)}\exp\frac{\alpha_nz}{R}+D_n^{(j)}\exp\left(\frac{-\alpha_nz}{R}\right)\right]J_0\left(\frac{\alpha_nr}{R}\right),\quad j=1,2,3,\tag{11}$$

where α_n is the eigenvalue and satisfies the equation

$$\frac{\varepsilon_{\rm ox}R}{t'_{\rm ox}\varepsilon_{\rm si}}J_0(\alpha_n)-J_1(\alpha_n)\alpha_n=0,\tag{12}$$

$J_i(x)$ is the first kind Bessel function of the order i. Fourier-Bessel series coefficients $C_n^{(1)}$, $D_n^{(1)}$, $C_n^{(2)}$, $D_n^{(2)}$, $C_n^{(3)}$, and $D_n^{(3)}$ are determined by the following boundary conditions.

The potential at the source end is

$$\phi_1(r,z=0)=V_{\rm bi},\tag{13}$$

where $V_{\rm bi}$ is the built-in potential. The potential at the drain end is

$$\phi_3(r,z=L)=V_{\rm bi}+V_{\rm ds}.\tag{14}$$

The electrostatic potential at the interface of the three regions is continuous

$$\phi_1(r,z=L_1)=\phi_2(r,z=L_1),\tag{15}$$

$$\phi_2(r,z=L_1+L_2)=\phi_3(r,z=L_1+L_2).\tag{16}$$

The electric flux at the interface of the three regions is continuous

$$\left.\frac{\partial\phi_1(r,z)}{\partial z}\right|_{z=L_1}=\left.\frac{\partial\phi_2(r,z)}{\partial z}\right|_{z=L_1},\tag{17}$$

$$\left.\frac{\partial\phi_2(r,z)}{\partial z}\right|_{z=L_1+L_2}=\left.\frac{\partial\phi_3(r,z)}{\partial z}\right|_{z=L_1+L_2}.\tag{18}$$

Using the boundary condition (13)–(18), the resultant expression of Fourier–Bessel series coefficients $C_n^{(1)}$, $D_n^{(1)}$, $C_n^{(2)}$, $D_n^{(2)}$, $C_n^{(3)}$, and $D_n^{(3)}$ can be obtained as

$$C_n^{(1)} = \left[-T_n^{(1)} \exp\left(-\frac{\alpha_n L}{R}\right) + T_n^{(2)} \cosh \frac{\alpha_n (L_1 - L)}{R} + T_n^{(3)} \cosh \frac{\alpha_n (L_1 + L_2 - L)}{R} + T_n^{(4)} \right] \times \left(2 \sinh \frac{\alpha_n L}{R}\right)^{-1}, \tag{19}$$

$$D_n^{(1)} = \left[T_n^{(1)} \exp \frac{\alpha_n L}{R} - T_n^{(2)} \cosh \frac{\alpha_n (L_1 - L)}{R} - T_n^{(3)} \cosh \frac{\alpha_n (L_1 + L_2 - L)}{R} - T_n^{(4)} \right] \times \left(2 \sinh \frac{\alpha_n L}{R}\right)^{-1}, \tag{20}$$

$$C_n^{(2)} = \left\{ \left[-T_n^{(1)} + T_n^{(2)} \cosh \frac{\alpha_n L_1}{R} \right] \exp\left(-\frac{\alpha_n L}{R}\right) + T_n^{(3)} \cosh \frac{\alpha_n (L_1 + L_2 - L)}{R} + T_n^{(4)} \right\} \times \left(2 \sinh \frac{\alpha_n L}{R}\right)^{-1}, \tag{21}$$

$$D_n^{(2)} = \left\{ \left[T_n^{(1)} - T_n^{(2)} \cosh \frac{\alpha_n L_1}{R} \right] \exp \frac{\alpha_n L}{R} - T_n^{(3)} \cosh \frac{\alpha_n (L_1 + L_2 - L)}{R} - T_n^{(4)} \right\} \times \left(2 \sinh \frac{\alpha_n L}{R}\right)^{-1}, \tag{22}$$

$$C_n^{(3)} = \left\{ \left[-T_n^{(1)} + T_n^{(2)} \cosh \frac{\alpha_n L_1}{R} + T_n^{(3)} \cosh \frac{\alpha_n (L_1 + L_2)}{R} \right] \exp\left(-\frac{\alpha_n L}{R}\right) + T_n^{(4)} \right\} \times \left(2 \sinh \frac{\alpha_n L}{R}\right)^{-1}, \tag{23}$$

$$D_n^{(3)} = \left\{ \left[T_n^{(1)} - T_n^{(2)} \cosh \frac{\alpha_n L_1}{R} - T_n^{(3)} \cosh \frac{\alpha_n (L_1 + L_2)}{R} \right] \exp \frac{\alpha_n L}{R} - T_n^{(4)} \right\} \times \left(2 \sinh \frac{\alpha_n L}{R}\right)^{-1}, \tag{24}$$

with

$$T_n^{(1)} = V_{\text{bi}} S_n^{(0)} - S_n^{(1)}, \tag{25}$$

$$T_n^{(2)} = S_n^{(2)} - S_n^{(1)}, \tag{26}$$

$$T_n^{(3)} = S_n^{(3)} - S_n^{(2)}, \tag{27}$$

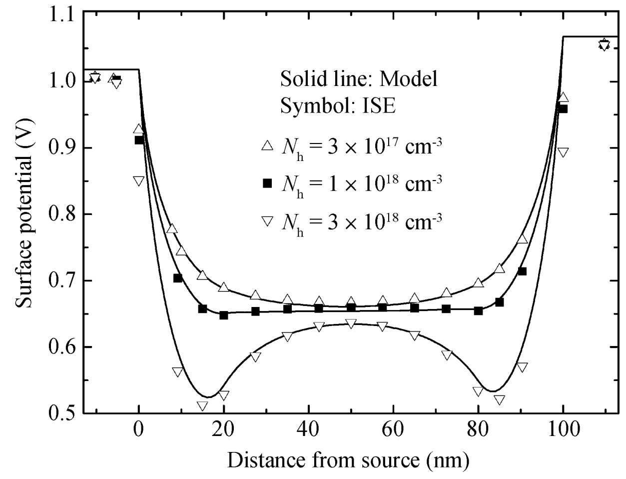

Fig. 2. Surface potential of HSG with various halo doping concentrations. The simulated device parameters are $V_{\text{gs}} = 0.2$ V, $V_{\text{ds}} = 0.05$ V, $R = 20$ nm, $t_{\text{ox}} = 2$ nm, $L_2 = 60$ nm and $L_1 = L_3 = 20$ nm.

$$T_n^{(4)} = (V_{\text{bi}} + V_{\text{ds}}) S_n^{(0)} - S_n^{(3)}, \tag{28}$$

where

$$S_n^{(0)} = \frac{2 J_1(\alpha_n)}{\alpha_n \left[J_1^2(\alpha_n) + J_0^2(\alpha_n) \right]}, \tag{29}$$

$$S_n^{(j)} = V_{\text{gs}} S_n^{(0)} + U_n^{(j)}, \tag{30}$$

$$U_n^{(j)} = -\left(\phi_{\text{MS}} + \frac{q N_j t'_{\text{ox}} R}{2 \varepsilon_{\text{ox}}} + \frac{q N_j R^2}{4 \varepsilon_{\text{si}}} \right) S_n^{(0)} + \frac{q N_j \left[R^2 \alpha_n J_1(\alpha_n) - 2 R^2 J_2(\alpha_n) \right]}{2 \varepsilon_{\text{si}} \left[J_1^2(\alpha_n) + J_0^2(\alpha_n) \right] \alpha_n^2}. \tag{31}$$

By differentiating the surface potential $\phi(r = R, z)$ with respect to z, the electric field $E(z)$ at the channel surface in the z direction is given as

$$E_j(z) = \sum_{n=1}^{\infty} \left[C_n^{(j)} \exp\left(\frac{\alpha_n z}{R}\right) - D_n^{(j)} \exp\left(\frac{-\alpha_n z}{R}\right) \right] \times \left(\frac{\alpha_n}{R}\right) J_0(\alpha_n), \quad j = 1, 2, 3. \tag{32}$$

2.2. Threshold voltage model

For HSG, the position of minimum surface potential depends on the halo doping concentration level. As Fig. 2 shows, the minimum surface potential lies in the region 2 when the halo doping concentration is not so heavy (e.g. $N_{\text{h}} = 3 \times 10^{17}$ cm^{-3}), while when the halo doping concentration is heavier (e.g. $N_{\text{h}} = 3 \times 10^{18}$ cm^{-3}), the minimum surface potential lies in the halo region near the source (region 1). To facilitate the calculation, derivative values of surface potential at the interface between region 1 and region 2 can be used to determine the position of minimum surface potential, i.e., if $\left.\frac{\partial \phi_1(r=R, z)}{\partial z}\right|_{z=L_1} > 0$, the minimum surface potential lies in the region 1, while $\left.\frac{\partial \phi_1(r=R, z)}{\partial z}\right|_{z=L_1} < 0$, the minimum surface potential lies in the region 2.

Due to rapid decay of the Bessel Fourier series coefficients, as shown in (19)–(24), the first term of them can dominate the

whole series[12], then the potential in region 1 and region 2 can be expressed as

$$\phi_1(r,z) = \left[C_1^{(1)} \exp\left(\frac{\alpha_1 z}{R}\right) + D_1^{(1)} \exp\left(-\frac{\alpha_1 z}{R}\right)\right] J_0\left(\frac{\alpha_1 r}{R}\right) + \frac{qN_1}{4\varepsilon_{\rm si}} r^2 + V_{\rm gs} - \phi_{\rm MS} - \frac{qN_1 t'_{\rm ox} R}{2\varepsilon_{\rm ox}} - \frac{qN_1 R^2}{4\varepsilon_{\rm si}}, \quad (33)$$

$$\phi_2(r,z) = \left[C_1^{(2)} \exp\left(\frac{\alpha_1 z}{R}\right) + D_1^{(2)} \exp\left(-\frac{\alpha_1 z}{R}\right)\right] J_0\left(\frac{\alpha_1 r}{R}\right) + \frac{qN_2}{4\varepsilon_{\rm si}} r^2 + V_{\rm gs} - \phi_{\rm MS} - \frac{qN_2 t'_{\rm ox} R}{2\varepsilon_{\rm ox}} - \frac{qN_2 R^2}{4\varepsilon_{\rm si}}. \quad (34)$$

When the minimum surface potential lies in region 1, by setting the first derivative of (33) at $r = R$ to zero, the minimum surface potential of region 1 and its related position can be achieved

$$z_{\min} = \frac{R}{2\alpha_1} \ln \frac{D_1^{(1)}}{C_1^{(1)}}, \quad (35)$$

$$\phi_1(r = R, z = z_{\min}) = 2\sqrt{C_1^{(1)} D_1^{(1)}} J_0(\alpha_1) + V_{\rm gs} - \phi_{\rm MS} - \frac{qN_1 t'_{\rm ox} R}{2\varepsilon_{\rm ox}}. \quad (36)$$

The threshold voltage is defined as the gate voltage that causes the minimum surface potential to become two times the Fermi potential, i.e.,

$$\phi_1(r = R, z = z_{\min}) = 2\phi_{\rm F}, \quad V_{\rm gs} = V_{\rm th}. \quad (37)$$

Substituting Eq. (36) into Eq. (37) and solving for $V_{\rm gs}$, the threshold voltage can be obtained.

$$V_{\rm th} = \frac{-\omega_2 + \sqrt{\omega_2^2 - 4\omega_1\omega_3}}{2\omega_1}, \quad (38)$$

with

$$\omega_1 = 4J_0^2(\alpha_1) Q_1 P_1 - 1, \quad (39)$$

$$\omega_2 = 4J_0^2(\alpha_1) Q_2 P_1 + 4J_0^2(\alpha_1) Q_1 P_2 + 2H, \quad (40)$$

$$\omega_3 = 4J_0^2(\alpha_1) Q_2 P_2 - H^2, \quad (41)$$

where

$$H = 2\phi_{\rm F} + \phi_{\rm MS} + \frac{qN_1 t'_{\rm ox} R}{2\varepsilon_{\rm ox}}, \quad (42)$$

$$Q_1 = \frac{\exp\left(-\frac{\alpha_1 L}{R}\right) - 1}{2\sinh\frac{\alpha_1 L}{R}}, \quad (43)$$

$$P_1 = \frac{1 - \exp\frac{\alpha_1 L}{R}}{2\sinh\frac{\alpha_1 L}{R}}, \quad (44)$$

$$Q_2 = \left\{ \left[U_1^{(1)} - V_{\rm bi} S_1^{(0)}\right] \exp\left(-\frac{\alpha_1 L}{R}\right) + T_1^{(2)} \cosh\frac{\alpha_1(L_1 - L)}{R} + T_1^{(3)} \cosh\frac{\alpha_1(L_1 + L_2 - L)}{R} + (V_{\rm bi} + V_{\rm ds}) S_1^{(0)} - U_1^{(3)} \right\} \left(2\sinh\frac{\alpha_n L}{R}\right)^{-1}, \quad (45)$$

$$P_2 = \left\{ \left[V_{\rm bi} S_1^{(0)} - U_1^{(1)}\right] \exp\frac{\alpha_1 L}{R} - T_1^{(2)} \cosh\frac{\alpha_1(L_1 - L)}{R} - T_1^{(3)} \cosh\frac{\alpha_1(L_1 + L_2 - L)}{R} - (V_{\rm bi} + V_{\rm ds}) S_1^{(0)} + U_1^{(3)} \right\} \left(2\sinh\frac{\alpha_n L}{R}\right)^{-1}. \quad (46)$$

When the minimum surface potential lies in region 2, the threshold voltage can be derived using the same method as above.

2.3. Subthreshold current calculation

Using the channel potential solution, the subthreshold current can be calculated. Since the current density J flows predominantly in the z direction from source to drain, the electron quasi-Fermi potential $\phi_{\rm n}(z)$ is essentially constant in the r direction. The current density (both drift and diffusion) can then be written as

$$J(r,z) = -q\mu_{\rm n} n(r,z) \frac{{\rm d}\phi_{\rm n}(z)}{{\rm d}z}, \quad (47)$$

where $n(r,z)$ is the carrier concentration and $\mu_{\rm n}$ is the electron mobility. By integrating the current density $J(r,z)$ through the circular cross section area in polar coordinates, the subthreshold current with respect to z can be expressed as

$$I_{\rm DS}(z) = q\mu_{\rm n} \frac{d\phi_{\rm n}(z)}{dz} \times 2\pi \int_0^R r n_{\rm i} \exp\{q[\phi(r,z) - \phi_{\rm n}(z)]/kT\} {\rm d}r. \quad (48)$$

By integrating Eq. (48) with respect to z from 0 to L, the subthreshold current can be obtained as[11]

$$I_{\rm DS} = \frac{\mu_{\rm n} kT (n_{\rm i}^2/N_{\rm a})\{1 - \exp[-V_{\rm DS}/(kT/q)]\}}{\displaystyle\int_0^L \frac{1}{2\pi \int_0^R r \exp[\phi(r,z)/(kT/q)]{\rm d}r} {\rm d}z}. \quad (49)$$

Then the subthreshold current can be calculated as a function of $V_{\rm gs}$ and $V_{\rm ds}$. A constant mobility model ($\mu_{\rm n}$ = 1417 cm^2/(V·s)) is used in both the analytical model and the 3D ISE simulation.

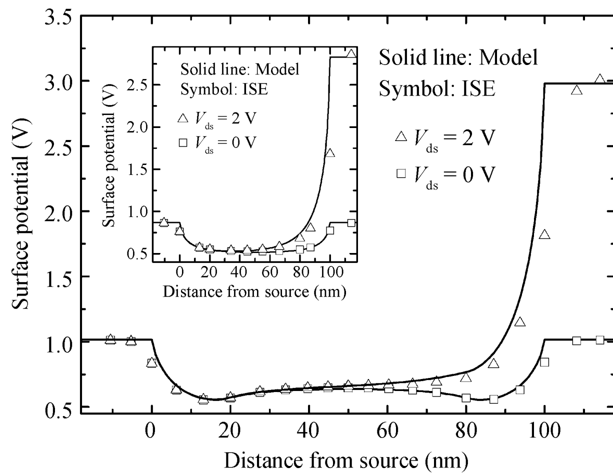

Fig. 3. Surface potential profile of HSG and USG (inset) with different V_{ds}. The simulated device parameters are $V_{gs} = 0.2$ V, $R = 20$ nm, $t_{ox} = 2$ nm, $L_2 = 60$ nm, $L_1 = L_3 = 20$ nm and $N_h = 2 \times 10^{18}$ cm^{-3}.

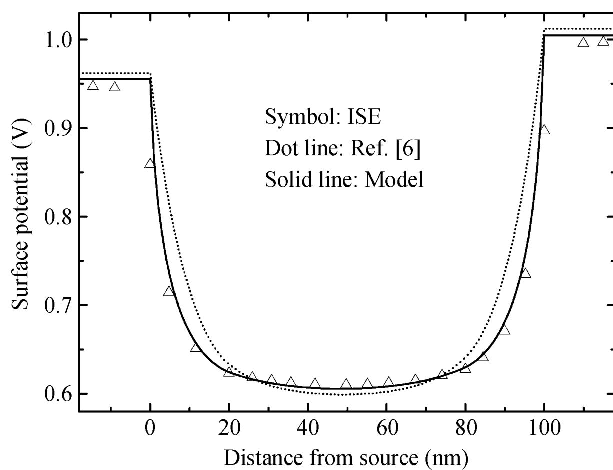

Fig. 4. Surface potential profile along the channel length with the model result from Ref. [6] for comparison. The simulated device parameters are $V_{gs} = 0.2$ V, $V_{ds} = 0.05$ V, $R = 20$ nm, $t_{ox} = 2$ nm, $L_2 = 60$ nm, $L_1 = L_3 = 20$ nm and $N_h = 3 \times 10^{17}$ cm^{-3}.

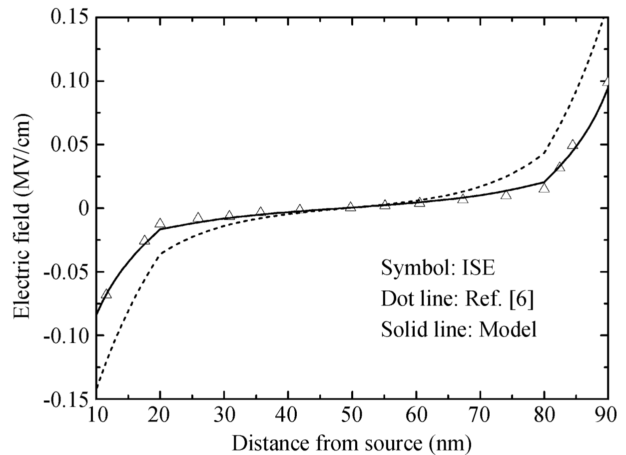

Fig. 5. Electrical field profile along the channel length with the model result from Ref. [6] for comparison. The simulated device parameters are $V_{gs} = 0.2$ V, $V_{ds} = 0.05$ V, $R = 20$ nm, $t_{ox} = 2$ nm, $L_2 = 60$ nm, $L_1 = L_3 = 20$ nm and $N_h = 3 \times 10^{17}$ cm^{-3}.

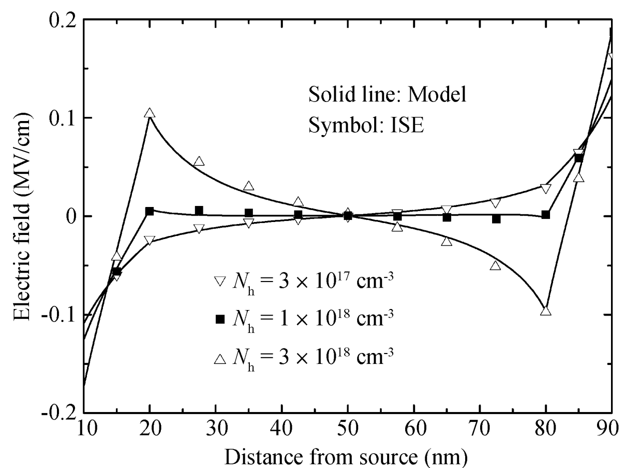

Fig. 6. Electrical field of HSG with various halo doping concentration. The simulated device parameters are $V_{gs} = 0.2$ V, $V_{ds} = 0.05$ V, $R = 20$ nm, $t_{ox} = 2$ nm, $L_2 = 60$ nm and $L_1 = L_3 = 20$ nm.

3. Results and discussion

Using derived analytical models, the performance of HSG is examined in terms of surface electrostatics potential, electric field distribution, threshold voltage roll-off and DIBL. The simulated data of uniformly doped surrounding-gate MOSFETs (USG) and results using models from Ref. [6] are also included for comparison. To verify the analytical model, the 3D device simulator ISE is employed to simulate the device characteristics. Unless otherwise stated, the drain and source doping concentration $N_d = 10^{19}$ cm^{-3}, silicon channel doping concentration $N_a = 10^{16}$ cm^{-3}, the work function of the metal gate is 4.65 V.

To gain an insight into the physical mechanism responsible for the improved performance of the HSG structure, Figure 3 shows the surface potential profile for HSG and USG (inset) with the different drain biases. It can be seen from the figure that due to the presence of the halo-doped regions, the surface potential profile of HSG near the source and drain end is lowered. As a result, there is no significant change in the minimum surface potential of HSG near the source end as the drain bias (V_{ds}) is increased even up to 2.0 V. For USG, however, the surface potential of the channel is severely affected by the drain voltage. As the drain bias increases, the position of the minimum surface potential is shifting toward the source while the minimum channel potential is pulled up, which causes intense SCEs. Therefore, the HSG structure exhibits better immunity to SCEs than the USG structure.

Figure 4 and 5 show the surface potential profile and electric field profile along the channel length, respectively. The model results from Ref. [6] are also included for comparison. It is clear that our model is superior to that proposed in Ref. [6] owing to the better agreement between the calculated results of our model and those of the simulation. In contrast to our approach, the PPA method causes a considerable deviation from the simulation results, especially near the source/drain end.

The electric field of HSG with different halo doping con-

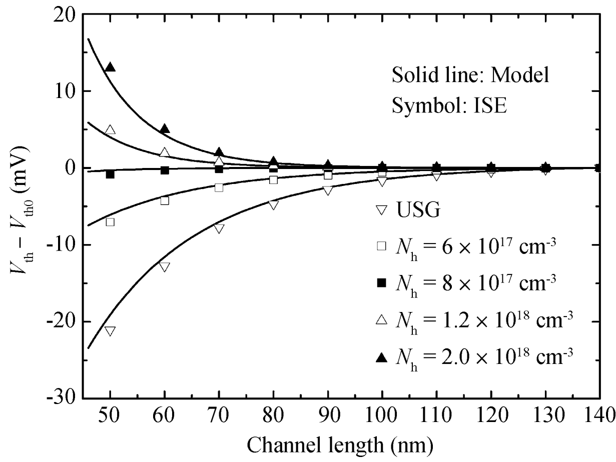

Fig. 7. Threshold voltage roll-off of USG and HSG with various halo doping concentration. The simulated device parameters are $V_{ds} = 0.05$ V, $R = 20$ nm, $t_{ox} = 2$ nm and $L_1 = L_3 = 20$ nm.

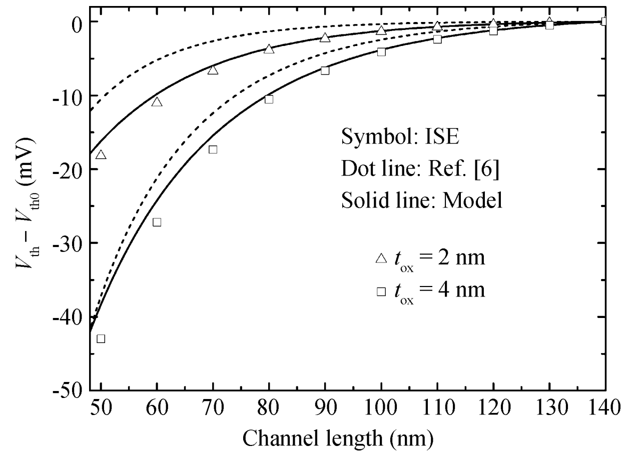

Fig. 9. Threshold voltage roll-off of HSG with various gate oxide thicknesses. The simulated device parameters are $V_{ds} = 0.05$ V, $R = 20$ nm, $N_h = 3 \times 10^{17}$ cm^{-3} and $L_1 = L_3 = 20$ nm.

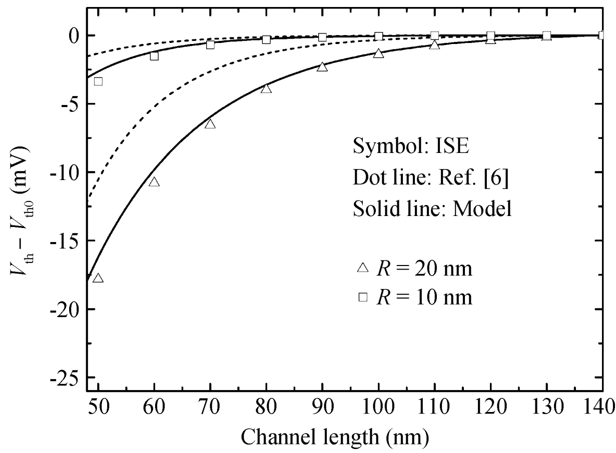

Fig. 8. Threshold voltage roll-off of HSG with various radii of silicon channel. The simulated device parameters are $V_{ds} = 0.05$ V, $t_{ox} = 2$ nm, $N_h = 3 \times 10^{17}$ cm^{-3} and $L_1 = L_3 = 20$ nm.

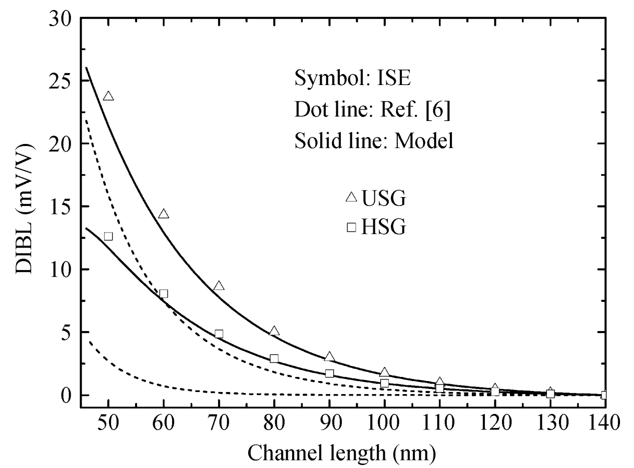

Fig. 10. DIBL variations in USG and HSG. The simulated device parameters are $R = 20$ nm, $t_{ox} = 2$ nm, $L_1 = L_3 = 20$ nm and $N_h = 6 \times 10^{17}$ cm^{-3}.

centration is shown in Fig. 6. It is found that too heavy halo doping concentration (e.g. $N_h = 3 \times 10^{18}$ cm^{-3}) will introduce two electric field peaks near the source and drain, which worsens HCEs. In contrast, a moderate halo doping concentration (e.g. $N_h = 1 \times 10^{18}$ cm^{-3}) reduces the electric field near source and drain and ensures better immunity to HCEs.

Figure 7 presents the threshold voltage roll-off of USG and HSG with various halo doping concentrations. It shows that the threshold voltage decreases rather faster in USG than in HSG when the gate length is below 80 nm, which indicates that HSG has better suppression of threshold roll-off than USG in the sub-100nm region. It also should be noted that when the halo doping concentration is too heavy, the threshold voltage roll-off reverses and becomes more positive as the channel length decreases. Therefore, a moderate halo doping concentration should be adopted to optimize the threshold voltage roll-off characteristic of HSG.

In Fig. 8, the threshold voltage roll-off of HSG is plotted with various radii of silicon channel. It is revealed that the small radius of the silicon channel leads to less threshold roll-off. However, when the radius of the silicon channel is less than 5nm, the quantum effects that cause different device characteristics will become important[13]. In this paper, we just address devices with a silicon channel radius larger than 5 nm, so quantum effects can be neglected.

It is shown in Fig. 9 that the threshold voltage roll-off of HSG with gate oxide thickness as a parameter. It can be observed that thick oxide leads to a larger threshold voltage roll-off. This is because thick oxide will resist a vertical electric field from the metal gate into the channel, resulting in degradation of gate controllability and threshold behavior[14]. Therefore, to suppress the threshold voltage roll-off, thin gate oxide is preferred.

Note that in Fig. 8 and Fig. 9, smaller $R : t_{ox}$ ratios have smaller differences between the PPA method and ISE simulation. In other words, when the $R : t_{ox}$ ratio is larger, the derivation of the PPA method becomes larger. This is because the 2D function $V(r, z)$ ignored in PPA has a Bessel function term $J_0(\frac{\alpha_n r}{R})$(see equation (11)), in which α_n is determined by the ratio of $R : t_{ox}$. When $R : t_{ox}$ ratio is larger, effects of 2D function become more obvious, hence leading to large errors

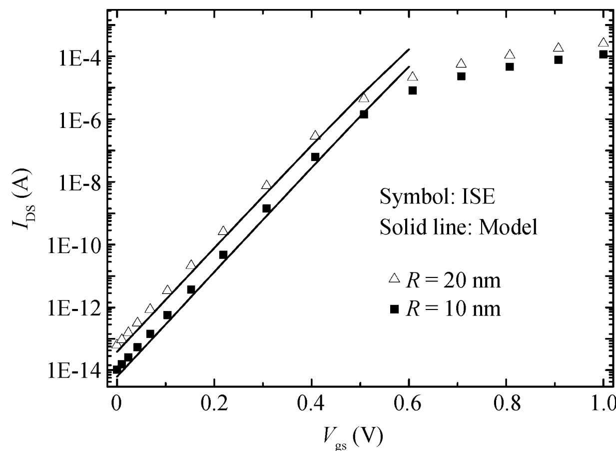

Fig. 11. Subthreshold current of HSG with various radii of silicon channel. The simulated device parameters are $V_{ds} = 0.05$ V, $t_{ox} = 2$ nm, $L_1 = L_3 = 20$ nm, $L_2 = 100$ nm and $N_h = 3 \times 10^{17}$ cm^{-3}.

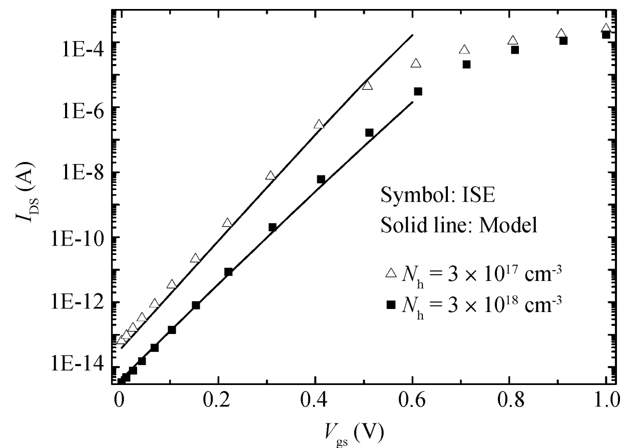

Fig. 12. Subthreshold current of HSG with various halo doping concentrations. The simulated device parameters are $V_{ds} = 0.05$ V, $R = 20$ nm, $t_{ox} = 2$ nm, $L_1 = L_3 = 20$ nm and $L_2 = 100$ nm.

in PPA method.

DIBL variations of USG and HSG are presented in Fig. 10. DIBL is defined as $\Delta V_{th}/\Delta V_{ds}$, where $\Delta V_{th} = V_{th}|_{V_{ds}=0.05} - V_{th}|_{V_{ds}=2}$. It is indicated that with two halo regions, the surface potential profile of HSG near the source and drain end is lowered, which ensures that the region near the source is screened from the drain bias variations, hence HSG accounts for better suppression of DIBL than USG.

Figures 8 to 10 also show that our calculated results are very close to those obtained from ISE, which demonstrate the superiority of our model over that proposed in Ref. [6].

The I_{DS}–V_{gs} curves calculated from Eq. (49) are compared with 3D numerical simulation results in Fig. 11 and Fig. 12. It is demonstrated that results obtained from the analytical solution agree well with the simulated results obtained using ISE in the subthreshold region. Figure 11 also shows the dependence of the subthreshold current on the gate bias with channel radius as a parameter. It can be observed that small radius has a lower subthreshold leakage current.

Subthreshold current of HSG with various halo doping concentrations is shown in Fig. 12. It is revealed that increasing the halo doping concentration can decrease the subthreshold current drastically. This is because, under subthreshold conditions, current conduction is dominated by diffusion and is controlled by the maximum barrier (minimum potential) along the channel. For HSG, the minimum potential is located in the halo region near the source end, therefore the subthreshold current is seriously affected by halo doping concentration.

4. Conclusion

Based on the exact 2D resultant solution of Poisson's equation, a new analytical model comprising electrostatic potential, electric field, threshold voltage and subthreshold current for halo-doped surrounding-gate MOSFETs is successfully developed. It is found that a new analytical model exhibits higher accuracy than that based on parabolic potential approximation when the thickness of the silicon channel is much greater than that of the oxide. It is also revealed that moderate halo doping concentration, thin gate oxide thickness and small silicon channel radius are needed to improve the threshold voltage characteristics. The results obtained from the analytical model agree well with the simulated results obtained using ISE. This paper not only provides an accurate analytical model for physical insight but also proposes a basic design guidance for HSG MOSFETs.

References

[1] Taur Y, Wann C H, Frank D J. 25 nm CMOS design considerations. IEDM Tech Dig, 1998: 789

[2] Jiménez D, Sáenz J J, Iñíguez B, et al. Modeling of nanoscale gate-all-around MOSFETs. IEEE Electron Device Lett, 2004, 25: 314

[3] Yu B, Lu W Y, Lu H, et al. Analytic charge model for surrounding-gate MOSFETs. IEEE Trans Electron Devices, 2007, 54: 492

[4] Hamid H A, Iñíguez B, Roig J. Analytical model of the threshold voltage and subthreshold swing of undoped cylindrical gate-all-around-based MOSFETs. IEEE Trans Electron Devices, 2007, 54: 572

[5] Liu F, He J, Zhang L N, et al. A charge-based model for long-channel cylindrical surrounding-gate MOSFETs from intrinsic channel to heavily doped body. IEEE Trans Electron Devices, 2008, 55: 2187

[6] Li Z C. Performance and analytical modeling of halo-doped surrounding gate MOSFETs. Chinese Physics B, 2008, 17: 4312

[7] He J, Zheng R, Zhang L N, et al. Continuous surface potential versus voltage equation of intrinsic surrounding-gate MOSFETs and analytic solution from accumulation to strong inversion region. Journal of Semiconductors, 2010, 31: 064001

[8] Choi B K, Jeong M K, Cho L H, et al. Current model of fully depleted nanoscale surrounding-gate metal–oxide–semiconductor field-effect transistors with doped channel in all operation regions. Jpn J Appl Phys, 2009, 48: 084501

[9] He J, Zhang J, Zhang L N, et al. A surface potential-based non-charge-sheet core model for undoped surrounding-gate MOSFETs. Journal of Semiconductors, 2009, 30: 024001

[10] Xiao D Y, Xie J, Chi M, et al. Simulation of gate-all-around cylindrical transistors for sub-10 nanometer scaling. Journal of Semiconductors, 2008, 29: 447

[11] Liang X P, Taur Y. A 2-D Analytical solution for SCEs in DG MOSFETs. IEEE Trans Electron Devices, 2004, 51: 1385

[12] Chiang T K. New analytical model for short-channel fully depleted dual-material-gate silicon-on-insulator metal–oxide–semiconductor field-effect transistors. Jpn J Appl Phys, 2010, 49: 074304

[13] Omura Y, Horiguchi S, Tabe M. Quantum-mechanical effects on the threshold voltage of ultrathin-SOI nMOSFETs. IEEE Electron Device Lett, 1993, 12: 569

[14] Chiang T K. A new compact subthreshold behavior model for dual-material surrounding gate (DMSG) MOSFETs. Solid-State Electron, 2009, 53: 490